


Research Article

Flexible 2D Cu Metal: Organic Framework@MXene Film Electrode with Excellent Durability for Highly Selective Electrocatalytic NH₃ Synthesis

Jing Wang,¹ Tao Feng,² Jiaxin Chen,¹ Jr-Hau He,³ and Xiaosheng Fang¹ 

¹Department of Materials Science, Fudan University, Shanghai 200433, China

²School of Chemical and Environmental Engineering, Shanghai Institute of Technology, Shanghai 201418, China

³Department of Materials Science and Engineering, City University of Hong Kong, Tat Chee Avenue, Kowloon, Hong Kong

Correspondence should be addressed to Jr-Hau He; jrhaue@cityu.edu.hk and Xiaosheng Fang; xshfang@fudan.edu.cn

Received 5 January 2022; Accepted 13 April 2022; Published 30 May 2022

Copyright © 2022 Jing Wang et al. Exclusive Licensee Science and Technology Review Publishing House. Distributed under a Creative Commons Attribution License (CC BY 4.0).

Electrocatalytic nitrate reduction to ammonia (ENRA) is an effective strategy to resolve environmental and energy crisis, but there are still great challenges to achieve high activity and stability synergistically for practical application in a fluid environment. The flexible film electrode may solve the abovementioned problem of practical catalytic application owing to the advantages of low cost, light weight, eco-friendliness, simple and scalable fabrication, extensive structural stability, and electrocatalytic reliability. Herein, 2D hybridization copper 1,4-benzenedi-carboxylate (CuBDC) has been grown on electronegative MXene nanosheets (Ti₃C₂T_x) seamlessly to prepare a 2D flexible CuBDC@Ti₃C₂T_x electrode for ENRA. The flexible electrode simultaneously exhibits high Faradaic efficiency (86.5%) and excellent stability for NH₃ synthesis, which are comparable to previously reported nanomaterials toward ENRA. Especially, the flexible electrode maintains outstanding FE_{NH_3} toward ENRA after the bending, twisting, folding, and crumpling tests, indicating excellent electroconductibility, high stability, and durability. This work not only provides mild permeation-mediated strategy to fabricate a flexible electrode but also explores the practical applications of the electrode with effectively environmental adaptability in solving global environmental contamination and energy crisis by effective ENRA.

1. Introduction

Ammonia (NH₃) is a potential hydrogen carrier due to its high energy density (4.32 kW·h/L) and storage capacity (17.6%) [1, 2]. However, it used to rely on the energy-intensive Haber–Bosch process (400–600°C, >400 atm) [3]. Recently, electrocatalytic N₂ reduction reaction (NRR) has been demonstrated as a potential approach for NH₃ generation [4] but a large amount of energy could be consumed to break the N≡N bond and the low solubility of N₂ in water limited the progress of the NRR [5, 6]. The nitrate (NO₃⁻) is selected as the most viable N source for NH₃ production due to its high solubility in water and lower energy consumption [7]. In addition, the NO₃⁻ is one of the most difficult N-pollutants to remove [8–10], which induces global eutrophication and does damage to the human health [11, 12]. Therefore, electrocatalytic NO₃⁻ reduction to NH₃ (ENRA) is one of the most promising strategy for producing

NH₃ under ambient conditions and solving global NO₃⁻ contamination and energy crisis [13, 14]. However, owing to the fragile nature of a traditional electrode, the practical application of ENRA is limited by poor stability and lossy and even disappeared activity after omnidirectional deformability in a fluid environment [14]. Thus, the electrocatalytic NH₃ synthesis using flexible electrode with effective electrocatalytic activity, high Faradaic efficiency, robust mechanical stability, and low environmental impacts would be a promising strategy to solve the abovementioned problem.

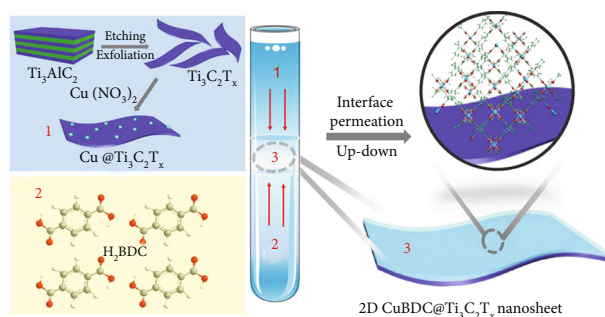
Recently, inspired by the increasing advantages of flexible fuel cell including being lightweight, portable, foldable/twistable, and wearable [15, 16], the two-dimensional (2D) materials have been reported as an ideal choice for constructing a flexible electrode because of the high aspect ratio of the nanostructure, with a transverse size expansion nanometer thickness [17]. Especially, the 2D MXenes have plenty of advantages for electrode preparation, such as high

electrical conductivity, flexibility, and hydrophilicity [18, 19]. In addition, MXenes are a kind of materials that can change the electronegativity of the active metal center, thus regulating the performance of the electrode [20, 21]. In addition to the metal-organic frameworks (MOFs), it can serve as a metal center in the catalyst and is an important type of porous coordination compounds [22]. Moreover, 2D MOF nanosheets with the thicknesses of several nanometers are expected to provide the large exposure to active atoms, as well as fast ion mass transfer [17]. For example, 2D copper- (Cu-) based conductive MOF is reported for aqueous CO_2 reduction reaction at low overpotentials with excellent catalytic activity [23], while NO_3^- reduction can also be catalyzed by the great potential of earth-abundant and cost-effective Cu-based electrode with high activity [24], which is comparable with scarce and high-cost noble metals [25–27]. Thus, the incorporation of 2D Cu MOFs with MXenes could synchronously enhance the ENRA performance, stability, electrical conductivity, flexibility, and eco-friendliness of the electrode [28]. Despite the benefits and demands, there is no report involving flexible electrodes for ENRA.

Based on the abovementioned discussion, in this report, the flexible 2D $\text{CuBDC}@Ti_3C_2T_x$ electrodes are designed by seamlessly coating the 2D CuBDC layer on the $Ti_3C_2T_x$ film using a simple permeation-mediated strategy under mild conditions (40°C), which are used for ENRA for the first time. The 2D flexible film structure is conducive to produce fully exposed active sites in contact with reaction solution, resulting in outstanding electrocatalytic activity and rapid reaction rate. The flexible electrodes exhibit excellent ENRA performance and mechanical stability. The reaction pathway and mechanism are demonstrated through online differential electrochemical mass spectrometry (DEMS). The following advantages can be achieved through our design: (1) superior mechanical flexibility and outstanding ENRA performance as well as high cyclic stability of the $\text{CuBDC}@Ti_3C_2T_x$, facilitating large-scale practical application of the flexible electrode; (2) comparable ENRA performance to noble metals, promoting their extensive commercialization due to the earth abundance and cost-effectiveness; (3) excellent stability and structural tunability after omnidirectional deformability of the flexible electrode-matching fluid environment for ENRA. For example, when the actual water flow changes greatly, the rigid electrode is easy to cause its efficiency reduction or even damage, while the flexible electrode with structural tunability can adapt to this environment well; and (4) free-standing and lightweight properties for portable electrocatalytic equipment.

2. Results and Discussion

The $\text{CuBDC}@Ti_3C_2T_x$ composite system is synthesized via permeation-mediated strategy, and $Ti_3C_2T_x$ nanosheets can be used as a template for the in situ 2D CuBDC growth. Firstly, the $Ti_3C_2T_x$ was synthesized from the Ti_3AlC_2 precursor in an etching solution containing hydrochloric acid (HCl) and lithium fluoride (LiF) [18]. Further shaking the etched $Ti_3C_2T_x$ resulted in a colloidal suspension of delami-



SCHEME 1: Schematic illustration of the preparation process of the 2D $\text{CuBDC}@Ti_3C_2T_x$ nanosheets as a flexible electrode via permeation-mediated strategy.

nated $Ti_3C_2T_x$ nanosheets in the pipe. Then, the 1,4-benzenedicarboxylic acid (H_2BDC) was placed in the bottom layer of the mixture of *N,N*-dimethyl formamide (DMF) and acetonitrile (CH_3CN) solution. $Ti_3C_2T_x$ nanosheets and $\text{Cu}(\text{NO}_3)_2$ were put on the upper layer of that solution, and these layers were separated vertically by an intermediate solvent layer according to different densities (Scheme 1). During static permeation, the functional groups ($-\text{OH}$ and $-\text{F}$) on $Ti_3C_2T_x$ nanosheets could absorb Cu^{2+} ions for the formation of $Ti_3C_2T_x-\text{Cu}$ via the electrostatic interaction. Then, the $Ti_3C_2T_x-\text{Cu}$ and H_2BDC solutions permeated each other at the intermediate solvent layer where the CuBDC crystals grow slowly on the $Ti_3C_2T_x$. Finally, CuBDC growth is restricted by the absence of $Ti_3C_2T_x-\text{Cu}$ which is in the latent organic phase and $\text{CuBDC}@Ti_3C_2T_x$ nanosheets were removed from the reaction by gravity.

The successful preparation of $Ti_3C_2T_x$ nanosheets is identified by the scanning electron microscope (SEM) images (Figure 1(a), Figure S1), transmission electron microscopy (TEM) images (Figure 1(d), Figure S2), STEM image, and energy dispersive X-ray spectroscopy (EDS) elemental mapping (Figure S3). The lattice spacing of $\sim 2.6 \text{ \AA}$ is obtained from the high-resolution transmission electron microscopy (HRTEM), which can be assigned to the (100) plane of $Ti_3C_2T_x$ (Figure S4). The crystal structures of the exfoliated $Ti_3C_2T_x$ nanosheets are confirmed by the X-ray diffraction (XRD) pattern (Figure S5). A typical morphological observation by atomic force microscopy (AFM) indicates that the $Ti_3C_2T_x$ nanosheets have lateral dimensions of several hundreds of nanometers with the thickness of $\sim 3 \text{ nm}$ (Figure S6), while the 2D CuBDC nanosheets exhibit a 2D-layered crystalline structure according to the SEM image (Figure 1(b)) and TEM image (Figure 1(e), Figure S7). The diffraction peaks observed in the XRD pattern further verify the crystal structure and composition of CuBDC (Figure 2(a)), which is in accordance with the previous report [17].

Because of the in situ growth of 2D CuBDC, the SEM image of $\text{CuBDC}@Ti_3C_2T_x$ displays the sheet-like morphology with surface roughness (Figure 1(c)). The TEM image of a hybridization nanosheet indicates that CuBDC is coated on the surfaces of $Ti_3C_2T_x$ nanosheets seamlessly (Figure 1(f)). The AFM image shows square nanosheets

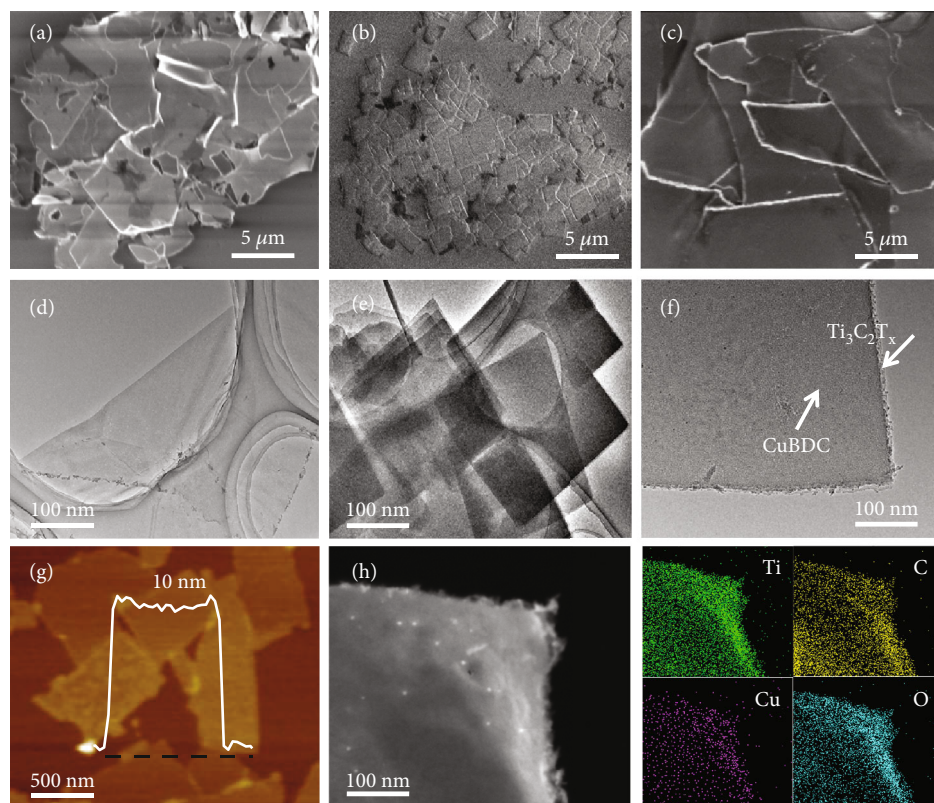


FIGURE 1: Morphology and structural analysis. SEM images of the (a) $\text{Ti}_3\text{C}_2\text{T}_x$, (b) CuBDC, and (c) CuBDC@ $\text{Ti}_3\text{C}_2\text{T}_x$ nanosheets. TEM images of the (d) $\text{Ti}_3\text{C}_2\text{T}_x$, (e) CuBDC, and (f) CuBDC@ $\text{Ti}_3\text{C}_2\text{T}_x$ nanosheets. (g) AFM image, (h) STEM image, and corresponding elemental mapping of Ti, C, Cu, and O of the CuBDC@ $\text{Ti}_3\text{C}_2\text{T}_x$ nanosheets.

with lateral dimensions of 0.6–3 μm and 8–12 nm thicknesses (Figure 1(g)). Furthermore, the STEM image with the corresponding EDS elemental mapping (Figure 1(h)) and the associated atom percentage spectrum (Figure S8 and Table S1) consistently confirm the successful synthesis of the 2D CuBDC@ $\text{Ti}_3\text{C}_2\text{T}_x$ with uniform distribution of Ti, Cu, C, and O elements throughout the nanosheets. In addition, bright particles presented in the STEM image of CuBDC@ $\text{Ti}_3\text{C}_2\text{T}_x$ are Cu nanoparticles. CuBDC is a coordination structure that can be easily destroyed to form Cu nanoparticles under intense electron beam bombardment of STEM.

The XRD patterns of $\text{Ti}_3\text{C}_2\text{T}_x$, CuBDC, and CuBDC@ $\text{Ti}_3\text{C}_2\text{T}_x$ are depicted in Figure 2(a). The observed diffraction peaks of CuBDC@ $\text{Ti}_3\text{C}_2\text{T}_x$ nanosheets located at 9.4, 11.7, 16.6, 28.8, and 42.4° are assigned to the (001), (222), (333), (442), and (882) planes of CuBDC, respectively [17, 29], while the peak located at 8.2° corresponds to the (002) plane of $\text{Ti}_3\text{C}_2\text{T}_x$ [18]. Three of the samples are analyzed by thermogravimetric analysis (TGA). As observed from TGA curves (Figure 2(b)), the CuBDC@ $\text{Ti}_3\text{C}_2\text{T}_x$ sample exhibits better thermal stability than that of CuBDC alone, suggesting that the in situ grow strategy significantly enhances the structural stability of the CuBDC@ $\text{Ti}_3\text{C}_2\text{T}_x$. The N_2 adsorption-desorption isotherms of the CuBDC and CuBDC@ $\text{Ti}_3\text{C}_2\text{T}_x$ reveal type-IV curves with a hysteresis loop ($P/P_0 = 1$), indicating that the pores on the electrocatalysts are dominantly mesopores (Figure 2(c)). As shown in

Figure 2(d), the pore size distribution of CuBDC obtained by the density functional theory (DFT) method displays the average pore size range of 3–13 nm. After seamlessly coating with $\text{Ti}_3\text{C}_2\text{T}_x$, the CuBDC@ $\text{Ti}_3\text{C}_2\text{T}_x$ exhibits a trimodal pore size distribution. Except for the similar mesopores of CuBDC (3 and ~12 nm), the CuBDC@ $\text{Ti}_3\text{C}_2\text{T}_x$ exhibits another mesopore with the size centered at ~20 nm. The results also show that CuBDC@ $\text{Ti}_3\text{C}_2\text{T}_x$ has larger surface areas of 161.45 m^2/g than that of CuBDC (95.13 m^2/g). As a result, the CuBDC@ $\text{Ti}_3\text{C}_2\text{T}_x$ shows an enlarged porous structure and specific surface area, which are beneficial to provide plentiful active sites and increase the electrode/electrolyte contact area [30].

The X-ray photoelectron spectroscopy (XPS) survey spectrum of CuBDC@ $\text{Ti}_3\text{C}_2\text{T}_x$ displays the main elements of C, O, Ti, and Cu, and the CuBDC and $\text{Ti}_3\text{C}_2\text{T}_x$ also are measured as control (Figure S9). For CuBDC@ $\text{Ti}_3\text{C}_2\text{T}_x$, the C 1s spectrum of CuBDC@ $\text{Ti}_3\text{C}_2\text{T}_x$ observes the presence of C–Ti (283 eV), C=C (285.6 eV), C–C (286.5 eV), C=O (288 eV), and O=C–O (289.7 eV) species (Figure 2(e)). Moreover, the O 1s spectrum detects the C=O (531 eV), O=C–O (532.4 eV), and –OH (533.6 eV) species (Figure 2(f)) [20]. Owing to the in situ growth of CuBDC on $\text{Ti}_3\text{C}_2\text{T}_x$ nanosheets, the change in C and O functional groups can be ignored, which is in line with the fact that $\text{Ti}_3\text{C}_2\text{T}_x$ kept its structural integrity after CuBDC growth (Figure S10) [31]. Fittings of the Cu 2p peaks of CuBDC@ $\text{Ti}_3\text{C}_2\text{T}_x$ results in the Cu^{2+} component with binding energy peaks located at 934.9 and 954.1 eV

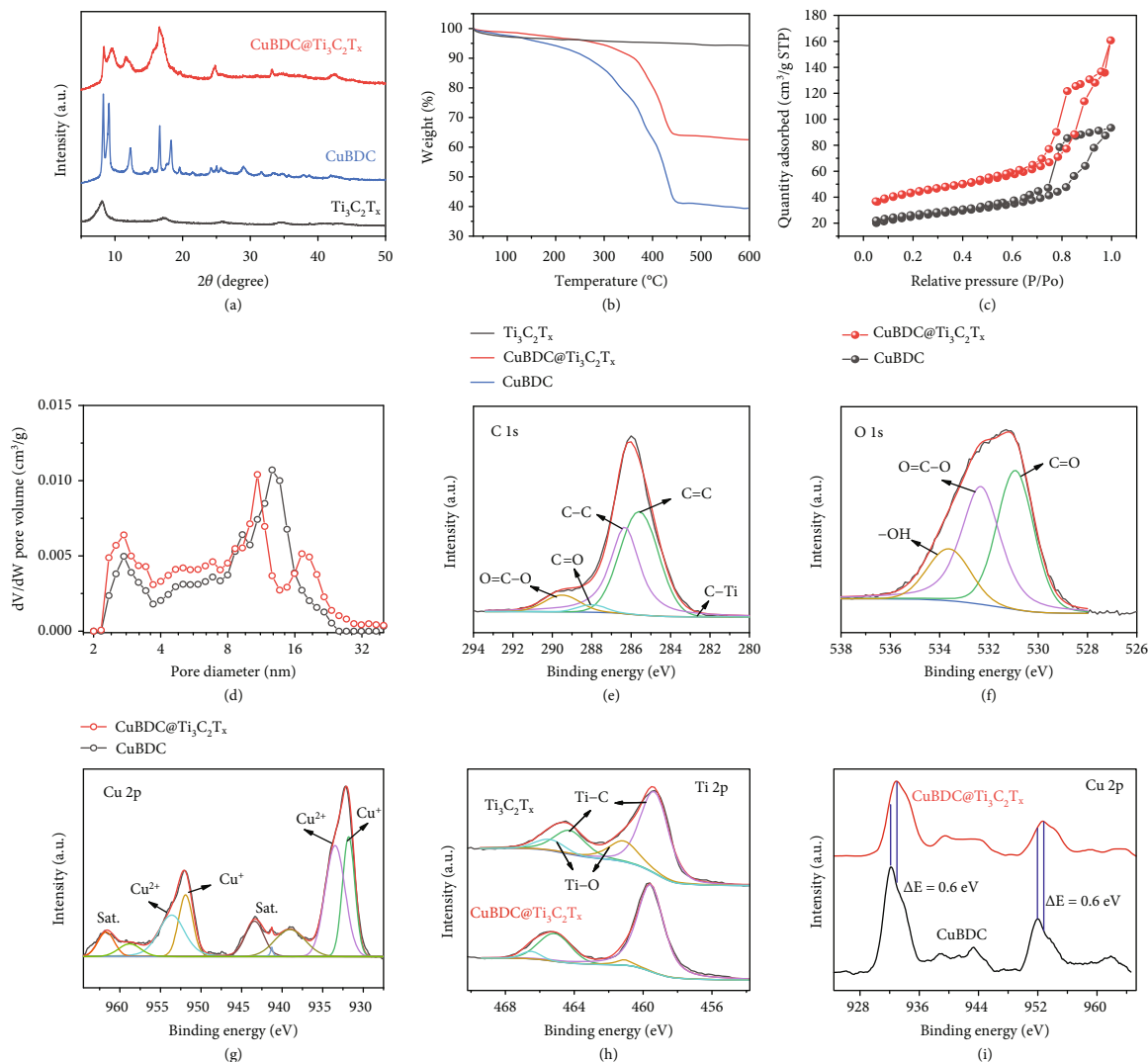


FIGURE 2: (a) XRD patterns and (b) TGA curves comparison of the $\text{Ti}_3\text{C}_2\text{T}_x$, CuBDC, and CuBDC@ $\text{Ti}_3\text{C}_2\text{T}_x$ nanosheets. (c) N_2 adsorption-desorption isotherms and (d) pore size distribution plots for CuBDC and CuBDC@ $\text{Ti}_3\text{C}_2\text{T}_x$ nanosheets. XPS analysis of CuBDC@ $\text{Ti}_3\text{C}_2\text{T}_x$ including (e) C 1s, (f) O 1s, and (g) Cu 2p spectra. The XPS comparison spectra of (h) Ti 2p in the $\text{Ti}_3\text{C}_2\text{T}_x$ and CuBDC@ $\text{Ti}_3\text{C}_2\text{T}_x$ and (i) Cu 2p in the CuBDC and CuBDC@ $\text{Ti}_3\text{C}_2\text{T}_x$, respectively.

while the surface Cu^+/Cu^0 species are assigned to 933.4 and 952.7 eV (Figure 2(g)). The Ti 2p XPS spectra of CuBDC@ $\text{Ti}_3\text{C}_2\text{T}_x$ indicate that Ti-C transferred to a higher bonding energy than the pristine $\text{Ti}_3\text{C}_2\text{T}_x$ (456.2 and 461.8 eV to 459.6 and 465.2 eV) (Figure 2(h)) [21]. This result confirms that the valence state and surface functional groups of Ti in CuBDC@ $\text{Ti}_3\text{C}_2\text{T}_x$ are changed with the gradual growth of CuBDC on the $\text{Ti}_3\text{C}_2\text{T}_x$ nanosheet, which suggests the strong interaction and charge transfer between $\text{Ti}_3\text{C}_2\text{T}_x$ and CuBDC [32]. As the oxidation state of Ti can affect the electrical conduction and ENRA performance, Ti-O/Ti-C should be considered properly. To verify the oxidation state of Ti, we have discussed the Ti-O/Ti-C during the CuBDC@ $\text{Ti}_3\text{C}_2\text{T}_x$ synthesis. Ti-O/Ti-C of CuBDC@ $\text{Ti}_3\text{C}_2\text{T}_x$ (21.4%) is lower than that of the origin $\text{Ti}_3\text{C}_2\text{T}_x$ (8.2%), which is largely because the functional groups (-OH) on $\text{Ti}_3\text{C}_2\text{T}_x$ nanosheets could absorb Cu^{2+} ions for the formation of $\text{Ti}_3\text{C}_2\text{T}_x\text{-Cu}$ via the electrostatic

interaction, and then, in situ CuBDC growth occurs. During the generation of CuBDC@ $\text{Ti}_3\text{C}_2\text{T}_x$, part of oxygen-containing groups is occupied, resulting in a decrease in the content of Ti-O. Moreover, the electronic structures of CuBDC and CuBDC@ $\text{Ti}_3\text{C}_2\text{T}_x$ are investigated to identify their intrinsic activity on the electrocatalysis. Compared to pure CuBDC, the Cu 2p_{3/2} XPS spectrum of CuBDC@ $\text{Ti}_3\text{C}_2\text{T}_x$ shifts to lower binding energy by 0.6 eV (Figure 2(i)), which indicates the electron transfer from $\text{Ti}_3\text{C}_2\text{T}_x$ to Cu at the interface of CuBDC@ $\text{Ti}_3\text{C}_2\text{T}_x$. Therefore, it can be concluded that the higher electron density of Cu leads to a decrease in the barrier reaction and a competitive inhibition of H_2 production [31], leading to excellent performances of CuBDC@ $\text{Ti}_3\text{C}_2\text{T}_x$ for ENRA.

The electrochemical tests are executed in a double-compartment cell to evaluate the ENRA performance of CuBDC@ $\text{Ti}_3\text{C}_2\text{T}_x$ (Figure S11). Varied potentials from -0.3 to -0.8 vs RHE are applied to choose the optimum

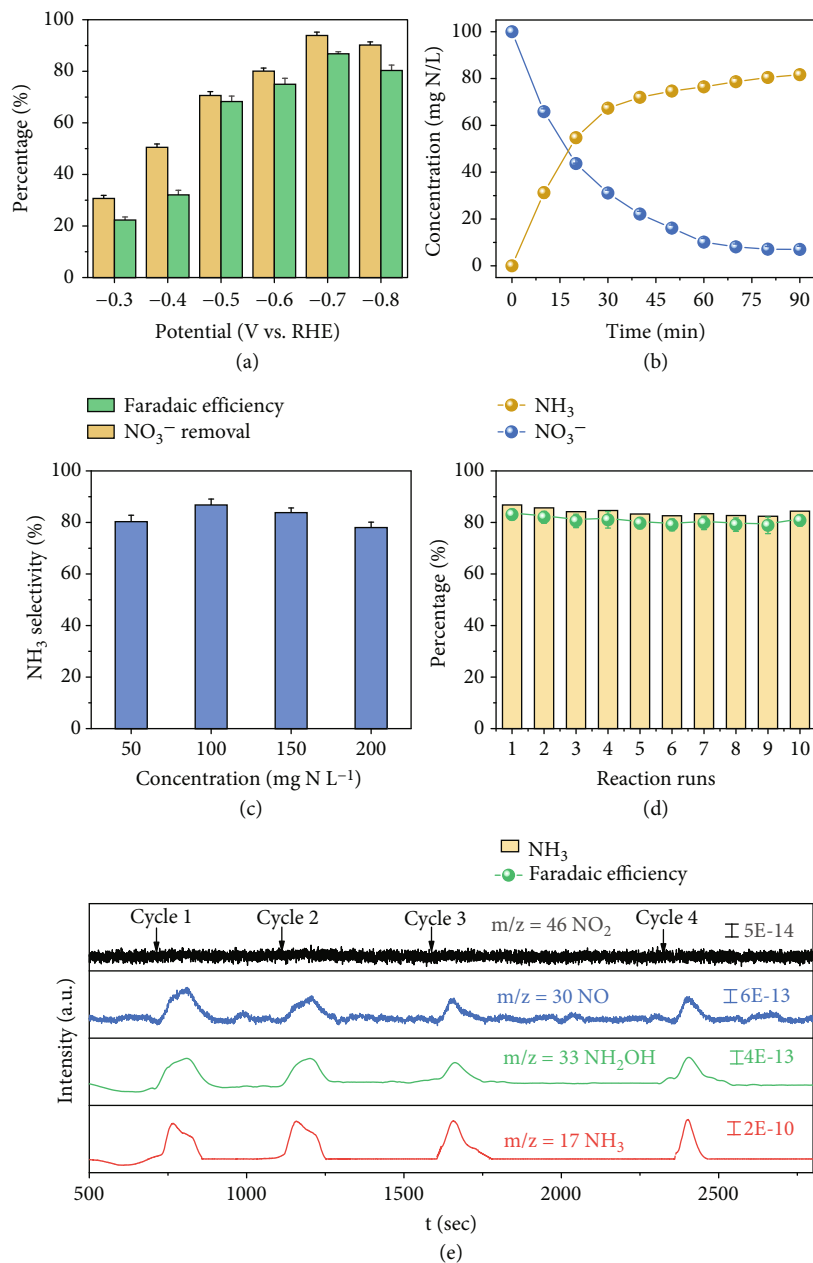


FIGURE 3: The electrocatalytic NO₃⁻ reduction to NH₃ (ENRA) performance based on the CuBDC@Ti₃C₂T_x. (a) The potential-dependent NO₃⁻ conversion efficiency and Faradaic efficiency, (b) time-dependent concentration change of NO₃⁻ and NH₃, (c) NH₃ selectivity versus different concentrations of NO₃⁻ at -0.7 V vs RHE, (d) the consecutive recycling tests of ENRA, and (e) DEMS measurements of ENRA of CuBDC@Ti₃C₂T_x (100 mg-N/L of NO₃⁻, 0.1 M Na₂SO₄).

one to ensure high performance of ENRA. As shown in Figure 3(a), the maximum NO₃⁻ conversion efficiency (93.1%) and FE_{NH_3} (86.5%) are obtained at -0.7 V instead of -0.8 V vs RHE. This result can be attributed to the occurrence of excessive hydrogen evolution reaction (HER) side reaction as indicated by literature results [33]. Thus, -0.7 V has been chosen as the operation voltage of subsequent batch experiment. As shown in Figure 3(b), the concentration of NH₃ produced on the CuBDC@Ti₃C₂T_x increases with the rapidly electrocatalytic reduction of NO₃⁻ below 10 mg-N/L (the maximum contaminant level limited by the World Health Organization [11]) within

50 min. As a comparison, the CuBDC electrode shows a significantly decreased NH₃ product and Ti₃C₂T_x exhibits neglectful NH₃ generation (Figure S12). When NO₃⁻ concentration increases from 50 to 200 mg-N/L, NH₃ selectivity remains basically unchanged, which reveals that the concentration is applicable to a wide range of the CuBDC@Ti₃C₂T_x (Figure 3(c)). The NH₃ selectivity and Faradaic efficiency retain more than 80% after 10 cycles of ENRA on the CuBDC@Ti₃C₂T_x (Figure 3(d)). Ti-O/Ti-C of CuBDC@Ti₃C₂T_x after ENRA reaction (9.3%) (Figure S13) is slightly higher than that of the origin CuBDC@Ti₃C₂T_x (8.2%). In ENRA reaction, Ti may be oxidized by NO₃⁻ but

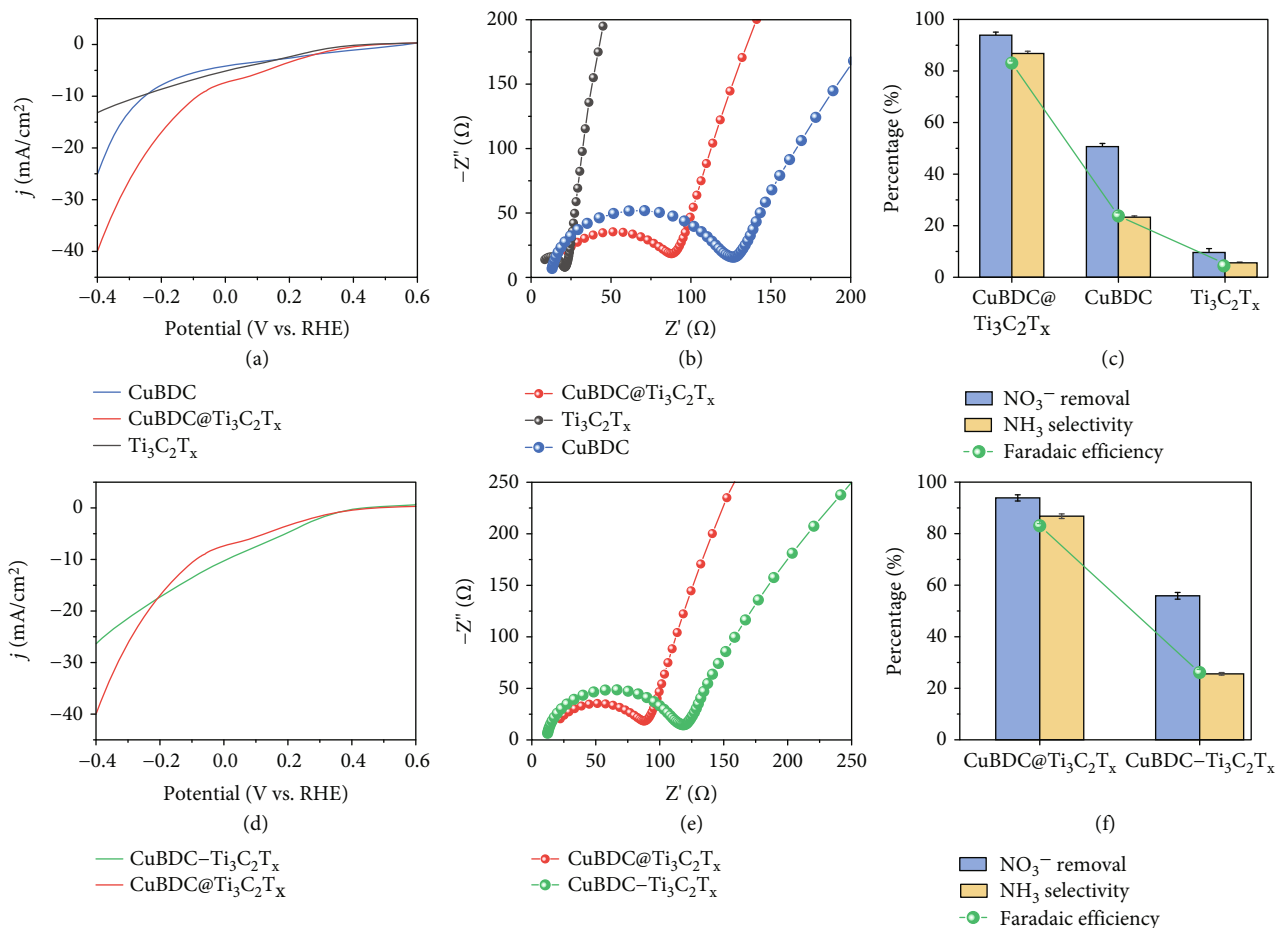


FIGURE 4: (a) LSV curves, (b) EIS plots, and (c) ENRA performance of the electrodes modified by CuBDC, Ti₃C₂T_x, and CuBDC@Ti₃C₂T_x, respectively. (d) LSV curves, (e) EIS plots, and (f) ENRA performance of the electrodes modified by the physically mixed CuBDC-Ti₃C₂T_x and CuBDC@Ti₃C₂T_x (0.1 M Na₂SO₄ electrolyte, 100 mg-N/L NO₃⁻).

the electrons generated in situ in the electrochemical process can further reduce it, thus maintaining the stable state of Ti, which is conducive to maintaining its strong conductivity and is more conducive to the ENRA reaction. These results consistently demonstrated the excellent ENRA performance, high durability, and long-term stability of the CuBDC@Ti₃C₂T_x electrode.

Direct proof of NO₃⁻ to NH₃ during the ENRA is acquired by the online DEMS system. When the applied voltages are varied from 0.1 to -0.9 V vs RHE, signals at m/z values of 46 (NO₂), 30 (NO), 33 (NH₂OH), and 17 (NH₃) appear during four cycles (Figure 3(e)). The presence of m/z signals at 33 shows that typical fragments of NH₂OH are detected, which is supported by the previous report [24]. m/z of 17 may come from evaporating water, but the water fragments do not change with electric potential. Therefore, it is reasonable to assume that the ENRA process can be traced with the above-obtained signals. Therefore, m/z of 17 is the signal confirming the formation of NH₃. Based on the abovementioned results, it can be concluded that the reaction pathway of ENRA is as follows: NO₃⁻ → NO₂⁻ → NO → NH₂OH → NH₃.

With the addition of NO₃⁻, the linear sweep voltammetry (LSV) curves of CuBDC@Ti₃C₂T_x, CuBDC, and Ti₃C₂T_x

all show the obvious increase in current density (Figure 4(a)). The CuBDC@Ti₃C₂T_x (-39.8 mA/cm²) appears higher current density than those of CuBDC (-24.9 mA/cm²) and Ti₃C₂T_x (-13.1 mA/cm²) at -1.0 V vs RHE. The fitting electrochemical impedance spectroscopy (EIS) data elucidate that the CuBDC@Ti₃C₂T_x generates a smaller arc radius than the CuBDC after adding the Ti₃C₂T_x nanosheets, pointing to remarkable improved charge transfer kinetics (Figure 4(b)). This result demonstrates that Ti₃C₂T_x is an ideal 2D nanomaterial to improve the electronic conductivity of the electrode. Compared with those of the Ti₃C₂T_x, the cyclic voltammetry (CV) curves of the CuBDC@Ti₃C₂T_x and CuBDC show obvious reduction and oxidation peaks (Figure S14). To reveal the advantages of the designed CuBDC@Ti₃C₂T_x, the ENRA performances of the CuBDC and Ti₃C₂T_x are also conducted for comparison. As shown in Figure 4(c), the CuBDC@Ti₃C₂T_x obtains higher NO₃⁻ conversion efficiency, NH₃ selectivity, and FE_{NH_3} than CuBDC (51.6%, 22.3%, and 21.8%, respectively) and Ti₃C₂T_x (9.6%, 5.1%, and 5.3%, respectively). These contrasts consistently demonstrate that the in situ growth of CuBDC on Ti₃C₂T_x nanosheets not only provides plentiful active sites but also enhances electronic conductivity, leading to

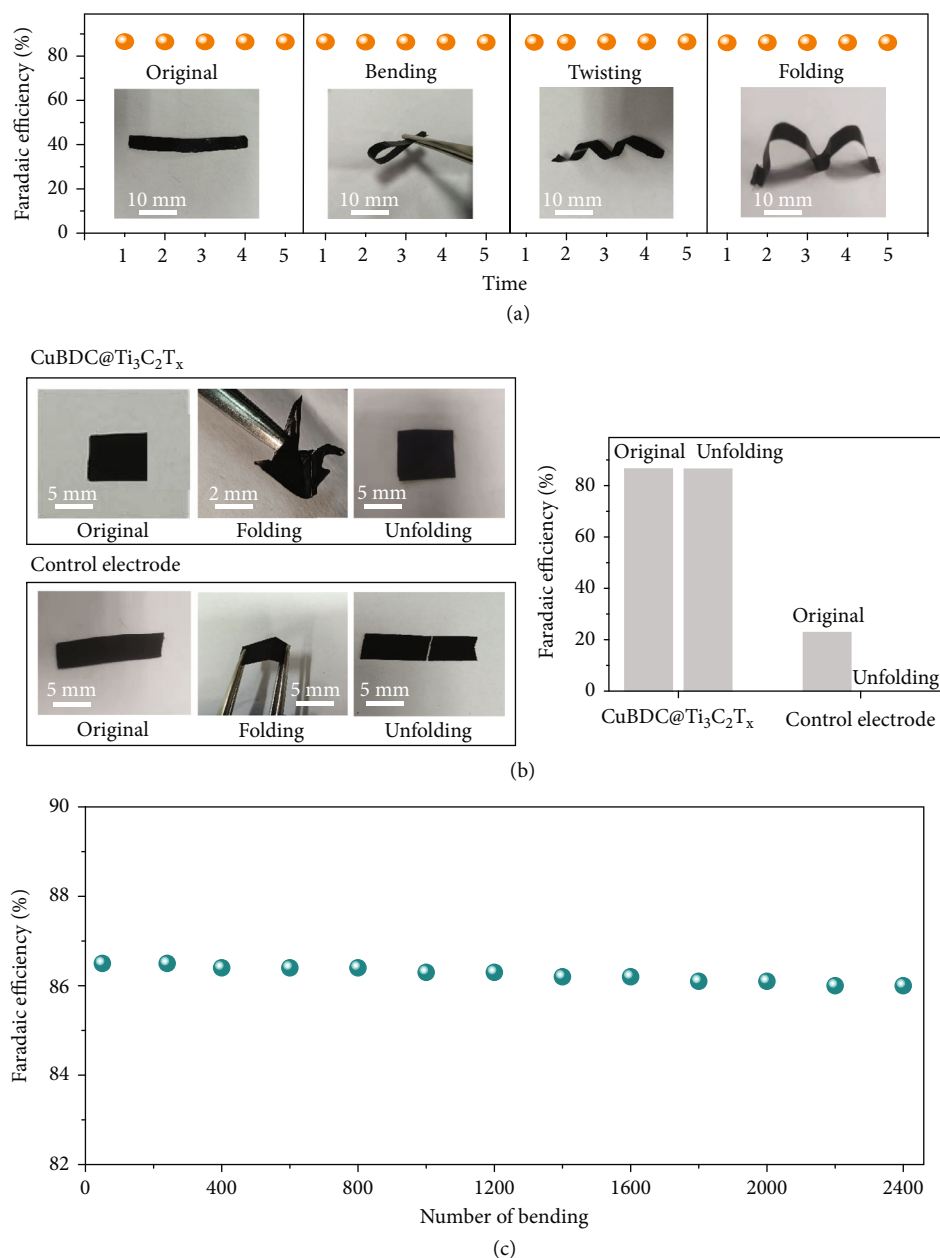


FIGURE 5: Mechanical deformability of the flexible CuBDC@Ti₃C₂T_x film electrode. (a) Change in Faradaic efficiency under various deformation modes: original, bending, twisting, and multifolding. (b) Photographs and ENRA performance comparison of flexible CuBDC@Ti₃C₂T_x electrode versus control electrode under original and unfolding. (c) Vary in Faradaic efficiency under various cycle testing of the flexible electrode after a number of bending.

accelerated electron transfer and improved electrocatalytic activity for ENRA. In addition, the ENRA performance of CuBDC@Ti₃C₂T_x is comparable to or even better than other previous reported electrodes (Table S2, S3) [34–39].

Compared with the CuBDC@Ti₃C₂T_x, the LSV curves of CuBDC–Ti₃C₂T_x exhibit lower current density (Figure 4(d)) and the EIS measurements also show that the larger the arc radius, the worse the charge transfer kinetics (Figure 4(e)). Moreover, the physically mixed CuBDC–Ti₃C₂T_x shows typical overlap nanosheets (Figure S15) and significantly decreased NO₃[–] conversion efficiency (50.7%), NH₃ selectivity (23.3%), and Faradaic efficiency (22.8%)

(Figure 4(f)). The LSV curves of CuBDC@Ti₃C₂T_x show the obvious increase of the current density in the presence of NO₃[–] in 0.1 M Na₂SO₄ electrolytes, but no current density is generated in the absence of NO₃[–] (Figure S16). Furthermore, the CuBDC@Ti₃C₂T_x produces higher current density than CuBDC and Ti₃C₂T_x electrodes with the addition of NO₃[–] (Figure S17). These results consistently indicate that the flexible CuBDC@Ti₃C₂T_x electrode shows specific response to the NO₃[–], leading to excellent ENRA performance.

Based on the abovementioned experimental results, the outstanding ENRA performances of the CuBDC@Ti₃C₂T_x may be due to the synergistic coupling effects of the 2D

CuBDC and $Ti_3C_2T_x$ components. The CuBDC provides plentiful active sites and porous structure while the $Ti_3C_2T_x$ nanosheets provide a flexible support to prevent the aggregation of catalytic sites, thus increasing the exposure of active surfaces and pore structures. When the CuBDC@ $Ti_3C_2T_x$ is used for ENRA, the hydrophilic $Ti_3C_2T_x$ assists in facilitating the easy access of NO_3^- to the Cu-active species (Figure S18) [32]. Moreover, the $Ti_3C_2T_x$ provides high electronic density, which not only reduces the reaction barrier but also suppresses the competing HER [31]. Thus, the hybridization of CuBDC@ $Ti_3C_2T_x$ can be used for highly selective electrocatalytic synthesis of NH_3 with high Faradaic efficiency.

The mechanical flexibility of the flexible CuBDC@ $Ti_3C_2T_x$ electrode is quantitatively examined under various deformation modes. The flexible CuBDC@ $Ti_3C_2T_x$ electrode retains good ENRA performance after bending, twisting, and folding (Figure 5(a)). This result demonstrates that omnidirectional deformability of the electrode has almost no effect on the ENRA performance. The mechanical flexibility of the CuBDC@ $Ti_3C_2T_x$ electrode is highlighted by comparing it with that of the mixed CuBDC- $Ti_3C_2T_x$ on the C film (CuBDC- $Ti_3C_2T_x$ -C). Notably, after folding and then unfolding, there is no significant change on the morphology and ENRA performance observed for the flexible CuBDC@ $Ti_3C_2T_x$ electrode, while the CuBDC- $Ti_3C_2T_x$ -C is easily broken and loses electrocatalytic activity (Figure 5(b)). This result indicates that the seamless growth of 2D CuBDC on $Ti_3C_2T_x$ nanosheets significantly improves mechanical flexibility for extending the electrocatalytic performance of the flexible CuBDC@ $Ti_3C_2T_x$ electrode. Moreover, the CuBDC@ $Ti_3C_2T_x$ film still maintains high FE_{NH_3} after bending for 2400 cycles, which confirms that the flexible electrode has high stability and durability during application in the fluid environment (Figure 5(c)). As a result, the CuBDC layers provide fully exposed active centers and pore structure for ENRA while the $Ti_3C_2T_x$ nanosheets endow the electrode with high electrical conductivity and mechanical flexibility, which enable the flexible CuBDC@ $Ti_3C_2T_x$ electrode to own highly electrocatalytic activity and cycling stability.

3. Conclusion

In summary, a flexible 2D free-standing CuBDC@ $Ti_3C_2T_x$ electrode with low resistance and tunable morphology is successfully prepared via permeation-mediated strategy. The fabricated film electrode owns the benefits of simple and scalable fabrication, excellent flexibility, extensive structural stability, low cost, light weight, and eco-friendliness for practical electrocatalytic application. The high NO_3^- conversion efficiency, NH_3 selectivity, and Faradaic efficiency of ENRA are obtained on the flexible electrode, which are comparable to the nanocatalysts based on precious metals previously reported. In particular, the omnidirectional deformability of the film electrode has neglectful effect on the ENRA performance, indicating excellent flexibility, stability, and durability. The reaction mechanism and pathway of the ENRA are demonstrated by the analysis results of online DEMS. This CuBDC@ $Ti_3C_2T_x$ film exhibits a plenti-

ful porous structure, large active surface area, high electrical conductivity, and superb mechanical flexibility, which can significantly improve the electrocatalytic activity and stability for effective environmental adaptability of the flexible electrode toward ENRA in the fluid environment.

4. Material and Methods

4.1. Materials. Copper nitrate trihydrate ($Cu(NO_3)_2 \cdot 3H_2O$, 99%), 1,4-benzenedicarboxylic acid (H_2BDC , 98%), sodium nitrate ($NaNO_3$, 99%), sodium nitrite ($NaNO_2$, 99%), ammonium chloride (NH_4Cl , 99%), sodium sulfate (Na_2SO_4 , 99%), acetylene black, acetonitrile (CH_3CN , 99%), NaOH (96%), HCl (36-38%), N, N-dimethylformamide (DMF, 99.5%), sulfamic acid, p-aminobenzenesulfonamide, N-(1-Naphthyl) ethylenediamine dihydrochloride, phosphoric acid, trichloromethane ($CHCl_3$, 99%), and Nessler's reagent are from Sino-pharm Chemical Reagent Co. Ltd. LiF (98.5%, 325 mesh, Alfa Aesar), Ti_3AlC_2 (98%, 400 mesh, 11 Technology Co. Ltd.), and all reagents were of analytical grade, and solutions were prepared by using ultrapure water (specific resistance of $18 M\Omega cm$).

4.2. Preparation of $Ti_3C_2T_x$ Nanosheets. 1 g of LiF was added into 20 mL 9 M HCl solution under stirring for 30 min. Subsequently, 1 g of Ti_3AlC_2 powder was slowly added into the solution in 5 minutes and the mixed solution was further stirred for 24 h at $40^\circ C$. After etching, the resultant solution was separated via centrifugation with washing (10 min at 3500 rpm), and then, the supernatant was decanted, followed by the addition of ultrapure water and 5 min handshaking. The washing process was repeated several times until the supernatant became dark-green and the pH was around 6.

4.3. Synthesis of CuBDC. A glass tube with 14 mm of the inner diameter was used to synthesize CuBDC nanosheets. Dissolve 30 mg H_2BDC in 2 mL DMF and 1 mL CH_3CN mixture at the bottom of the tube. In this solution, carefully add a mixture of 1 mL DMF and 1 mL CH_3CN to prevent the premature mixture of the two solutions. Finally, 30 mg $Cu(NO_3)_2 \cdot 3H_2O$ is dissolved in a mixture of 1 mL DMF and 2 mL CH_3CN and carefully add it to the top layer tube. After leaving the tube to react in static conditions at $40^\circ C$ for 24 h, the formation of a blue precipitate was observed at the bottom of the tube, which was collected by centrifugation at 8000 rpm and consecutively washed 3 times with 1 mL of DMF followed by another 3 times with 1 mL of $CHCl_3$ and dried in a vacuum oven at $50^\circ C$ for 12 h.

4.4. Fabrication of the Flexible CuBDC@ $Ti_3C_2T_x$ Electrode. The fabrication method for CuBDC@ $Ti_3C_2T_x$ was similar to that of the CuBDC, except that 10 mg of $Ti_3C_2T_x$ nanosheets along with 30 mg $Cu(NO_3)_2 \cdot 3H_2O$ was added to the top layer (mixture of 1 mL DMF and 2 mL of CH_3CN).

4.5. Material Characterizations. The SEM (Gemini SEM 500), TEM (Talos F200X), STEM (Talos F200X) with EDS, and AFM measurement (Bruker Dimension Edge atomic force microscope) were conducted to investigate the morphologies of samples. XPS spectra (ESCALAB 250Xi) were measured

using the Mg $K\alpha$ line as the excitation source. XRD patterns (Bruker D8 ADVANCE) were recorded with an X-ray diffractometer. TGA (Waters Discovery) was introduced to determine the thermal properties in a N_2 atmosphere in which the heating rate is $5^\circ\text{C}/\text{min}$. N_2 adsorption-desorption data were obtained from the Micromeritics ASAP2020M analyzer. Density functional theory (DFT) is used to calculate the pore size distribution. The DEMS (QAS 100) data were collected in the online gas analysis.

4.6. Electrochemical Measurements. ENRA experiments were conducted on a three-electrode system in H-type membrane-separated electrolyte cells using a CHI 660D electrochemical workstation. Pt wire and Ag/AgCl electrodes were used as counter and reference electrode. All potentials in contrast to reversible hydrogen electrode (RHE) were recorded. Potential E was converted to the RHE: $E(\text{versus RHE}) = E(\text{versus Ag/AgCl}) + 0.197\text{V} + 0.059\text{V} \times \text{pH}$. LSV curves were performed at a rate of $100\text{mV}/\text{s}$ from 0 to -1.0V vs RHE. Current densities were standard in the geometrical area, and the AC impedance technique was employed to study the electrochemical impedance spectra (EIS) with the $\text{CuBDC}@Ti_3C_2T_x$, CuBDC, $Ti_3C_2T_x$, and $\text{CuBDC}-Ti_3C_2T_x$ -based electrodes. The range of frequency was set from 100 MHz to 1000 Hz. Nitrate solutions (20 mL) with varied initial concentrations (50–200 mg·N/L) were prepared using 200 mg·N/L stock solution and then were added into the cathode cell. Na_2SO_4 (0.1 M) as the electrolyte was evenly distributed to the cathode and anode cell. Application of the Amperometric $i-t$ technique was conducted at constant potential (ambient conditions within 90 minutes at -0.7V vs RHE) [40]. All experiments were carried out in triplicate. ENRA experiments of CuBDC, $Ti_3C_2T_x$, and physical mixed $\text{CuBDC}-Ti_3C_2T_x$ were performed as control to determine the superiority of $\text{CuBDC}@Ti_3C_2T_x$ electrodes under the same conditions.

Data Availability

All data needed to evaluate the conclusions in the paper are presented in the paper and/or the Supplementary Materials. Additional data related to this paper may be requested from the authors.

Conflicts of Interest

The authors declare no conflict of interest.

Authors' Contributions

Xiaosheng Fang, Jing Wang, and Tao Feng designed the project and experimented. Jing Wang, Tao Feng, and Jiixin Chen prepared and characterized the materials. Jing Wang and Tao Feng wrote the manuscript supported by Xiaosheng Fang and Jr-Hau He. Jiixin Chen, Ziliang Li, and Hui Liu revised the article. All authors contributed to the data analysis and discussed and commented on the manuscript.

Acknowledgments

The authors would like to thank Drs. Ziliang Li and Hui Liu for their valuable discussions. This work is supported by the National Key R&D Program of China (nos. 2018YFA0703700 and 2017YFA0204600), National Natural Science Foundation of China (nos. 12061131009 and 51872050), and Science and Technology Commission of Shanghai Municipality (nos. 21520712600 and 19520744300).

Supplementary Materials

Determination of NO_3^- -N, determination of NO_2^- -N, determination of NH_3 -N, and calculation of the conversion rate, selectivity, and Faradaic efficiency. Figure S1: the SEM image of the $Ti_3C_2T_x$ nanosheets. Figure S2: the TEM image of the $Ti_3C_2T_x$ nanosheets. Figure S3: the SEM image and corresponding EDS elemental mapping of Ti, C, O, F, and element overlay of the $Ti_3C_2T_x$ nanosheets. Figure S4: the HRTEM image of $Ti_3C_2T_x$ nanosheets with the corresponding SAED pattern. Figure S5: XRD pattern of $Ti_3C_2T_x$ nanosheets. Figure S6: AFM pattern of the $Ti_3C_2T_x$ nanosheets. Figure S7: the TEM image of the CuBDC nanosheets. Figure S8: EDS spectrum of the $\text{CuBDC}@Ti_3C_2T_x$ nanosheets. Figure S9: the XPS survey spectra of $\text{CuBDC}@Ti_3C_2T_x$, $Ti_3C_2T_x$, and CuBDC witness the main elements of Ti, C, O, and Cu. Figure S10: the XPS analysis of $Ti_3C_2T_x$ including the (a) C 1s, (b) Ti 2p, (c) O 1s, and (d) F 1s spectra. Figure S11: the photo of double-compartment cell for electrocatalytic nitrate reduction to ammonia based on the flexible 2D $\text{CuBDC}@Ti_3C_2T_x$ film electrode. Figure S12: the time-dependent concentration change of NO_3^- and NH_3 for ENRA reaction based on the (a) CuBDC and (b) $Ti_3C_2T_x$ electrodes. Figure S13: the XPS comparison spectra of Ti 2p in $\text{CuBDC}@Ti_3C_2T_x$ after ENRA. Figure S14: the CV plots of the $\text{CuBDC}@Ti_3C_2T_x$, CuBDC, and $Ti_3C_2T_x$ electrodes. Figure S15: the TEM image of the $\text{CuBDC}-Ti_3C_2T_x$ nanosheets. Figure S16: the LSV curves of the electrodes modified by $\text{CuBDC}@Ti_3C_2T_x$ in 0.1 M Na_2SO_4 electrolytes with or without NO_3^- (100 mg·N/L). Figure S17: LSV curves of (a) CuBDC and (b) $Ti_3C_2T_x$ in 0.1 M Na_2SO_4 electrolytes with or without NO_3^- (100 mg·N/L). Figure S18: schematic illustration of the possible reaction pathways at $\text{CuBDC}@Ti_3C_2T_x$ for ENRA. Table S1: the atom percentage of the $\text{CuBDC}@Ti_3C_2T_x$ nanosheets. Table S2: comparison of ammonia selectivity by electrocatalytic nitrate reduction reported in the literatures. Table S3: comparison of FENH3 and NH_3 yield rates by electrocatalytic nitrate reduction reported in the literatures. (*Supplementary Materials*)

References

- [1] B. H. R. Suryanto, H.-L. Du, D. Wang, J. Chen, A. N. Simonov, and D. R. MacFarlane, "Challenges and prospects in the catalysis of electroreduction of nitrogen to ammonia," *Nature Catalysis*, vol. 2, no. 4, pp. 290–296, 2019.
- [2] L. Hollevoet, M. De Ras, M. Roeyers, J. Hofkens, and J. A. Martens, "Energy-efficient ammonia production from air and water using electrocatalysts with limited Faradaic efficiency," *ACS Energy Letters*, vol. 5, no. 4, pp. 1124–1127, 2020.

- [3] W. Ren, Z. Mei, S. Zheng et al., "Wavelength-dependent solar N_2 fixation into ammonia and nitrate in pure water," *Research*, vol. 2020, article 3750314, p. 12, 2020.
- [4] H. Wang, Y. Chen, R. Fan et al., "Selective electrochemical reduction of nitrogen to ammonia by adjusting the three-phase interface," *Research*, vol. 2019, article 1401209, p. 12, 2019.
- [5] X. Cui, C. Tang, and Q. Zhang, "A review of electrocatalytic reduction of dinitrogen to ammonia under ambient conditions," *Advanced Energy Materials*, vol. 8, no. 22, article 1800369, 2018.
- [6] Y. Liu, M. Cheng, Z. He et al., "Pothole-rich ultrathin WO_3 nanosheets that trigger $N\equiv N$ bond activation of nitrogen for direct nitrate photosynthesis," *Angewandte Chemie International Edition*, vol. 58, no. 3, pp. 731–735, 2019.
- [7] V. Rosca, M. Duca, M. T. De Groot, and M. T. Koper, "Nitrogen cycle electrocatalysis," *Chemical Reviews*, vol. 109, no. 6, pp. 2209–2244, 2009.
- [8] N. Gruber and J. N. Galloway, "An Earth-system perspective of the global nitrogen cycle," *Nature*, vol. 451, no. 7176, pp. 293–296, 2008.
- [9] D. E. Canfield, A. N. Glazer, and P. G. Falkowski, "The evolution and future of Earth's nitrogen cycle," *Science*, vol. 330, no. 6001, pp. 192–196, 2010.
- [10] J. Wang, Z. Deng, T. Feng, J. Fan, and W. X. Zhang, "Nanoscale zero-valent iron (nZVI) encapsulated within tubular nitride carbon for highly selective and stable electrocatalytic denitrification," *Chemical Engineering Journal and the Biochemical Engineering Journal*, vol. 417, article 129160, 2021.
- [11] J. Wang, L. Ling, Z. Deng, and W. X. Zhang, "Nitrogen-doped iron for selective catalytic reduction of nitrate to dinitrogen," *Science Bulletin*, vol. 65, no. 11, pp. 926–933, 2020.
- [12] Y. Lan, H. Luo, Y. Ma, Y. Hua, T. Liao, and J. Yang, "Synergy between copper and iron sites inside carbon nanofibers for superior electrocatalytic denitrification," *Nanoscale*, vol. 13, no. 22, pp. 10108–10115, 2021.
- [13] N. Barrabés and J. Sá, "Catalytic nitrate removal from water, past, present and future perspectives," *Applied Catalysis B: Environmental*, vol. 104, no. 1–2, pp. 1–5, 2011.
- [14] J. Wang, T. Feng, J. Chen et al., "Electrocatalytic nitrate/nitrite reduction to ammonia synthesis using metal nanocatalysts and bio-inspired metalloenzymes," *Nano Energy*, vol. 86, article 106088, 2021.
- [15] Z. Li, M. K. Joshi, J. Chen, Z. Zhang, Z. Li, and X. Fang, "Mechanically compatible UV photodetectors based on electrospun free-standing Y^{3+} -doped TiO_2 nanofibrous membranes with enhanced flexibility," *Advanced Functional Materials*, vol. 30, no. 52, article 2005291, 2020.
- [16] Z. Li, F. Davar, J. Chen, Z. Li, and X. Fang, "CdS/CdSO₄ nanoflower-based photodetector with enhanced photoelectric performances," *ACS Applied Nano Materials*, vol. 3, no. 10, pp. 10190–10199, 2020.
- [17] T. Rodenas, I. Luz, G. Prieto et al., "Metal-organic framework nanosheets in polymer composite materials for gas separation," *Nature Materials*, vol. 14, no. 1, pp. 48–55, 2015.
- [18] J. Chen, Z. Li, F. Ni, W. Ouyang, and X. Fang, "Bio-inspired transparent MXene electrodes for flexible UV photodetectors," *Materials Horizons*, vol. 7, no. 7, pp. 1828–1833, 2020.
- [19] W. Song, J. Chen, Z. Li, and X. Fang, "Self-powered MXene/GaN van der Waals heterojunction ultraviolet photodiodes with superhigh efficiency and stable current outputs," *Advanced Materials*, vol. 33, no. 27, article e2101059, 2021.
- [20] L. Zhao, B. Dong, S. Li et al., "Interdiffusion reaction-assisted hybridization of two-dimensional metal-organic frameworks and Ti_3C_2Tx nanosheets for electrocatalytic oxygen evolution," *ACS Nano*, vol. 11, no. 6, pp. 5800–5807, 2017.
- [21] C. Cui, R. Cheng, H. Zhang et al., "Ultrastable MXene@Pt/SWCNTs' nanocatalysts for hydrogen evolution reaction," *Advanced Functional Materials*, vol. 30, no. 47, article 2000693, 2020.
- [22] T. Feng, Y. Wang, Y. N. Wu, D. M. Kabtamu, K. László, and F. Li, "A feasible linker transformation strategy towards the formation of Cu_2O nanoparticles for immobilization in hierarchical CuBTC for adsorption desulfurization," *Journal of Materials Chemistry A*, vol. 8, no. 17, pp. 8678–8683, 2020.
- [23] L. Majidi, A. Ahmadiparidari, N. Shan et al., "2D copper tetrahydroxyquinone conductive metal-organic framework for selective CO_2 electrocatalysis at low overpotentials," *Advanced Materials*, vol. 33, no. 10, article 2004393, 2021.
- [24] Y. Wang, W. Zhou, R. Jia, Y. Yu, and B. Zhang, "Unveiling the activity origin of a copper-based electrocatalyst for selective nitrate reduction to ammonia," *Angewandte Chemie International Edition*, vol. 59, no. 13, pp. 5350–5354, 2020.
- [25] J. Li, G. Zhan, J. Yang et al., "Efficient ammonia electrosynthesis from nitrate on strained ruthenium nanoclusters," *Journal of the American Chemical Society*, vol. 142, no. 15, pp. 7036–7046, 2020.
- [26] J. Yang, P. Sebastian, M. Duca, T. Hoogenboom, and M. T. Koper, "pH dependence of the electroreduction of nitrate on Rh and Pt polycrystalline electrodes," *Chemical Communications*, vol. 50, no. 17, pp. 2148–2151, 2014.
- [27] J.-X. Liu, D. Richards, N. Singh, and B. R. Goldsmith, "Activity and selectivity trends in electrocatalytic nitrate reduction on transition metals," *ACS Catalysis*, vol. 9, no. 8, pp. 7052–7064, 2019.
- [28] J. Park, A. C. Hinckley, Z. Huang et al., "Synthetic routes for a 2D semiconductive copper hexahydroxybenzene metal-organic framework," *Journal of the American Chemical Society*, vol. 140, no. 44, pp. 14533–14537, 2018.
- [29] C. G. Carson, K. Hardcastle, J. Schwartz et al., "Synthesis and structure characterization of copper terephthalate metal-organic frameworks," *European Journal of Inorganic Chemistry*, vol. 2009, no. 16, pp. 2338–2343, 2009.
- [30] Q. Zhang, F. Yue, L. Xu, C. Yao, R. D. Priestley, and S. Hou, "Paper-based porous graphene/single-walled carbon nanotubes supported Pt nanoparticles as freestanding catalyst for electro-oxidation of methanol," *Applied Catalysis B: Environmental*, vol. 257, article 117886, 2019.
- [31] P. Li, M. Wang, X. Duan et al., "Boosting oxygen evolution of single-atomic ruthenium through electronic coupling with cobalt-iron layered double hydroxides," *Nature Communications*, vol. 10, no. 1, p. 1711, 2019.
- [32] T. Y. Ma, J. L. Cao, M. Jaroniec, and S. Z. Qiao, "Interacting carbon nitride and titanium carbide nanosheets for high-performance oxygen evolution," *Angewandte Chemie International Edition*, vol. 55, no. 3, pp. 1138–1142, 2016.
- [33] H. Xu, J. Wu, W. Luo, Q. Li, W. Zhang, and J. Yang, "Dendritic cell-inspired designed architectures toward highly efficient electrocatalysts for nitrate reduction reaction," *Small*, vol. 16, no. 30, article e2001775, 2020.

- [34] L. Wang, M. Li, C. Feng et al., "Ti nano electrode fabrication for electrochemical denitrification using Box- Behnken design," *Journal of Electroanalytical Chemistry*, vol. 773, pp. 13–21, 2016.
- [35] C. Li, K. Li, C. Chen, Q. Tang, T. Sun, and J. Jia, "Electrochemical removal of nitrate using a nanosheet structured $\text{Co}_3\text{O}_4/\text{Ti}$ cathode: effects of temperature, current and pH adjusting," *Separation and Purification Technology*, vol. 237, article 116485, 2020.
- [36] L. Mattarozzi, S. Cattarin, N. Comisso et al., "Electrochemical reduction of nitrate and nitrite in alkaline media at CuNi alloy electrodes," *Electrochimica Acta*, vol. 89, pp. 488–496, 2013.
- [37] D. Yin, Y. Liu, P. Song et al., "In situ growth of copper/reduced graphene oxide on graphite surfaces for the electrocatalytic reduction of nitrate," *Electrochimica Acta*, vol. 324, article 134846, 2019.
- [38] M. Chen, H. Wang, Y. Zhao et al., "Achieving high-performance nitrate electrocatalysis with PdCu nanoparticles confined in nitrogen-doped carbon coralline," *Nanoscale*, vol. 10, no. 40, pp. 19023–19030, 2018.
- [39] W. Li, C. Xiao, Y. Zhao, Q. Zhao, R. Fan, and J. Xue, "Electrochemical reduction of high-concentrated nitrate using Ti/TiO₂ nanotube array anode and Fe cathode in dual-chamber cell," *Catalysis Letters*, vol. 146, no. 12, pp. 2585–2595, 2016.
- [40] J. Zhang, S. Zhao, Y. Xu et al., "Nitrate stimulates anaerobic microbial arsenite oxidation in paddy soils," *Environmental Science and Technology*, vol. 51, no. 8, pp. 4377–4386, 2017.